

Cold Sintering of LLTO Composite Electrolytes for Solid-State Lithium Batteries

Aras Karapekmez,^[a, d] Yi-Chen Lan,^[b] Gulin Vardar,^[d] Nuri Ersoy,^[d] and Enrique D. Gomez^{*[a, b, c]}

Solid-state batteries have the potential for higher energy densities and enhanced safety when compared to conventional lithium-ion batteries. The perovskite-type $\text{Li}_{3x}\text{La}_{2/3-x}\text{TiO}_3$ (LLTO) is an attractive ceramic electrolyte due to its high ionic conductivity, broad electrochemical stability window, and thermal and chemical stability. The conventional sintering process for ceramics, typically performed at high temperatures ($\sim 1000^\circ\text{C}$), poses a critical bottleneck for integrating solid electrolytes with active electrode materials. In this study, $\text{Li}_{0.29}\text{La}_{0.57}\text{TiO}_3$ /polypropylene carbonate (PPC) composite electrolytes containing lithium perchlorate (LiClO_4) were densified using cold sintering at 125°C . The resulting LLTO-based composite electrolytes

exhibit relative densities above 80% and ionic conductivities exceeding $10^{-4} \text{ S cm}^{-1}$ at room temperature. The symmetric $\text{Li}/\text{LLTO-PPC-LiClO}_4/\text{Li}$ cell with PVDF interlayers achieves a high critical current density of 1.8 mA cm^{-2} at room temperature. Solid-state lithium batteries fabricated with LLTO composite solid electrolytes deliver a high discharge capacity of 151 mAh g^{-1} at 0.1 C and 135 mAh g^{-1} at 0.2 C . Our approach, which integrates ceramic and polymer materials, produces composite electrolytes with superior properties, highlighting the potential of cold sintering for advancing solid-state batteries.

1. Introduction

Lithium-ion batteries are critical for many applications, including electric vehicles.^[1] The electrolyte within conventional lithium-ion batteries comprises lithium salts dissolved in an organic solvent, forming a critical component that facilitates ion transfer, enabling energy storage and release.^[2] As lithium-ion batteries approach the upper limits of energy density using conventional cathode and anode materials, there is a growing demand for advanced electrode materials to achieve the necessary energy density in next-generation electronic devices.^[3] Batteries with lithium metal anodes are emerging as a promising solution to meet the high energy requirements of these next-generation devices due to their inherently superior properties, including high capacity and the lowest negative electrochemical potential.^[4] Using lithium metal, however, raises

safety concerns primarily due to the formation of needle-like dendrites between the anode and the liquid electrolyte, which result from uneven lithium metal dissolution and cause a short circuit of the battery.^[5] Furthermore, any chemical or thermal degradation in the separator can trigger uncontrolled reactions at the electrode-electrolyte interface, which can potentially cause excessive heat generation and lead to explosions and fires.^[6]

The flammability of liquid electrolytes has driven significant work to develop all-solid-state batteries for a wide range of applications.^[7] Solid-state batteries hold great promise to power next-generation devices, especially electric vehicles, because of their high energy density, reduced risk of fire and explosions, and improved electrochemical and thermal stability.^[8] Solid-state electrolytes are mainly composed of two classes of materials: organic or polymer-based electrolytes and inorganic ceramic-based electrolytes.^[9] Due to their intrinsic material properties, polymer electrolytes exhibit excellent flexibility, ease of fabrication, good electrochemical stability, and interfacial compatibility with existing anode and cathode materials. Nevertheless, the primary obstacle to the practical use of polymer electrolytes is their limited ionic conductivity, which is often lower than $10^{-5} \text{ S cm}^{-1}$ at room temperature.^[10]

As an alternative, oxide-based ceramic electrolytes offer significant advantages, including high ionic conductivity, a broad electrochemical stability window, compatibility with lithium metal anodes, resistance to dendrite formation, and superior thermal and chemical stability.^[11] Among oxide-based electrolytes, $\text{Li}_{3x}\text{La}_{2/3-x}\text{TiO}_3$ ($0.07 < x < 0.13$) (LLTO), $\text{Li}_7\text{La}_3\text{Zr}_2\text{O}_{12}$ (LLZO), and $\text{Li}_{1.3}\text{Al}_{0.3}\text{Ti}_{1.7}(\text{PO}_4)_3$ (LATP) have emerged as prominent candidates, each exhibiting unique properties in terms of electrochemical stability, ionic conductivity, and Young's modulus.^[12]

[a] A. Karapekmez, E. D. Gomez
Materials Research Institute, The Pennsylvania State University, University Park, PA 16802, USA
E-mail: edg12@psu.edu

[b] Y.-C. Lan, E. D. Gomez
Department of Chemical Engineering, The Pennsylvania State University, University Park, PA 16802, USA

[c] E. D. Gomez
Department of Materials Science and Engineering, The Pennsylvania State University, University Park, PA 16802, USA

[d] A. Karapekmez, G. Vardar, N. Ersoy
Department of Mechanical Engineering, Bogazici University, Istanbul 34342, Turkey

 Supporting information for this article is available on the WWW under <https://doi.org/10.1002/batt.202400631>

 © 2024 The Author(s). *Batteries & Supercaps* published by Wiley-VCH GmbH. This is an open access article under the terms of the Creative Commons Attribution License, which permits use, distribution and reproduction in any medium, provided the original work is properly cited.

Nevertheless, the main challenge of oxide-based electrolytes is their densification, which necessitates a sintering process with temperatures exceeding 900 °C.^[13] High-temperature processing leads to several drawbacks, such as the formation of impurity phases, lithium loss, and high processing costs.^[14] Furthermore, the co-sintering with oxide-based electrolytes and readily accessible cathodes is performed at elevated temperatures to ensure intimate physical contact between the layers. Interfacial sintering above 500 °C, however, leads to the formation of lithium-ion blocking secondary phases and structural changes at the solid electrolyte/cathode interface induced by elemental diffusion.^[15]

Cold sintering can lower the sintering temperature to below 300 °C for various materials, including microwave dielectrics, ferroelectrics, semiconductors, and battery components.^[16–18] Cold sintering uses a transient solvent, applied pressure, and modest temperatures to achieve particle rearrangement, dissolution-precipitation, evaporation of the transient solvent, and grain growth or consolidation.^[19] This approach is amenable to various oxide-based electrolyte materials. Liu et al.^[20] explored the effects of solvent, applied pressure, and sintering conditions on the relative density and ionic conductivity of LATP. LATP solid electrolytes were sintered using different methods, including conventional high-temperature, dry-press, and cold sintering, using two different solvents: water and acetic acid. Using acetic acid as the solvent results in a fabricated pellet with a relative density of 93%, only 3% less than that of high-temperature sintering. Nevertheless, the ionic conductivity of LATP pellets fabricated through cold sintering using water or acetic acid was approximately one-tenth of the conductivity observed in conventionally sintered pellets. The high ionic conductivity observed during high-temperature sintering is attributed to a larger average grain size and well-defined, smooth grain boundaries.

Lee et al.^[14] incorporated bis(trifluoromethanesulfonyl)imide (LiTFSI) salts into LATP to address the high resistance at amorphous grain boundaries resulting from low processing temperatures of cold sintering. Highly dense microstructures were obtained for composite solid electrolytes with relative densities between 85% and 90%, depending on the amount of LiTFSI salt added. Moreover, LiTFSI salt at grain boundaries in LATP facilitated ion transport, effectively bridging the gap between grains and resulting in a high ionic conductivity of $10^{-4} \text{ S cm}^{-1}$ at room temperature.

Seo et al.^[21] demonstrate the benefit of adding dimethylformamide (DMF) during cold sintering of Mg- and Sr-doped LLZO solid electrolytes. PPC and LiClO₄ were used to prepare a polymer-salt solution by stirring them in acetonitrile for several hours. The binder solution was mixed with the synthesized solid electrolyte powder, and a small amount of dimethylformamide liquid agent was added as a plasticizer. Impedance measurements show that the presence of DMF in the as-prepared solution is critical for achieving desirable ionic conductivity in the LLZO-based composite electrolyte fabricated by cold sintering. The drastic change in the ionic conductivity was attributed to an increase in polymer conductivity, as the addition of DMF decreases the viscosity of the binding polymer,

and thereby facilitates the movement of ions in the polymer domains, which are localized to grain boundaries. He et al.^[22] introduced polyethylene-oxide (PEO)-LiTFSI mixtures into Ta-doped LLZO ($\text{Li}_{6.4}\text{La}_3\text{Zr}_{1.4}\text{Ta}_{0.6}\text{O}_{12}$) solid electrolytes to investigate how varying concentrations of polymer-lithium salt mixtures influence the ionic conduction mechanism in composite solid electrolytes. The solid electrolytes designated LLZTO-PEO_x-LiTFSI (where $x=1, 1.5, 2, 5$, and 8) were fabricated through cold sintering, using varying EO to Li molar ratios. LLZTO-PEO_x-LiTFSI exhibits a high ionic conductivity of $2.4 \times 10^{-4} \text{ S cm}^{-1}$ at room temperature. Their findings suggest that excessive polymer reduces the density of the composite electrolyte, resulting in lower densification and larger pores between particles. Therefore, when the molar ratio of EO: Li increases from 2–8, the ionic conductivity of the composite solid electrolyte decreases by about an order of magnitude.

In addition to the potential for composite fabrication, cold sintering could enable recycling of spent battery materials. Eliminating the need for high-temperature processing and the use of solvents to decompose materials into recoverable compounds is advantageous. Mechanical degradation is the primary failure mechanism in solid-state electrolytes,^[23] such that restoring the mechanical integrity of spent electrolytes enables their reuse in a battery cell. Lan et al.^[24] developed a direct reprocessing route for Mg- and Sr-doped LLZO-based composite solid electrolytes using cold sintering. PPC and LiClO₄ containing LLZO-based composites were reprocessed at 100 °C for 1 h under a uniaxial pressure of 250 MPa to regain densified microstructures, eliminating lithium-ion blocking structural defects induced upon cycling. Composite solid electrolytes exhibit relative densities of about 75% with ionic conductivities on the order of $10^{-4} \text{ S cm}^{-1}$ after 5 recycling cycles. Batteries with reprocessed electrolytes ($\text{LiFePO}_4/\text{Reprocessed LLZO-PPC-LiClO}_4/\text{Li}_4\text{Ti}_5\text{O}_{12}$) show a high discharge capacity of 168 mAh g⁻¹ at 0.1 C and excellent retention of capacity at 0.2 C for over 100 cycles. Furthermore, cold sintering enables the recycling of solid-state batteries by providing a route for reprocessing of the electrolyte, with recovery after recycling of 94% of initial capacity for cells with LTO based anodes and 92% for cells with Li metal based anodes.^[25]

Despite progress in processing of oxide electrolytes, cold sintering of the perovskite LLTO remains underexplored. Large grain boundary resistances are a common limitation of oxide-based ceramic electrolytes, including for garnet and NASICON-type materials.^[26] This issue is particularly severe in LLTO, posing a critical bottleneck to ionic conductivity. Previous work has reported that the conductivity at grain boundaries in LLTO can be 2–3 orders of magnitude lower than in the bulk, significantly limiting electrochemical performance.^[27] The ability to co-sinter ceramic and polymer materials with cold sintering could address this limitation, by providing alternative pathways for ion transport in LLTO composites.^[14]

Here, we fabricate ceramic-based composite electrolytes by integrating polymer-salt mixtures (PPC-LiClO₄) with LLTO using cold sintering at 125 °C. Cold sintered composites exhibit high relative densities above 80% and a high ionic conductivity of $3 \times 10^{-4} \text{ S cm}^{-1}$ at room temperature; the ionic conductivity was

high for temperatures between 0–100 °C, leading to a low activation energy of 0.25 eV. The symmetric Li/LLTO/Li cell with PVDF interlayers achieves a high critical current density of 1.8 mA cm⁻² at room temperature. Solid-state lithium batteries fabricated with LLTO-based composite solid electrolytes deliver a discharge capacity of 151 mAh g⁻¹ at 0.1 C and 135 mAh g⁻¹ at 0.2 C.

2. Results and Discussion

Cold sintering enables the densification of ceramic-based composites at modest temperatures (under 300 °C) by employing a transient solvent to facilitate mass transport.^[16] This approach not only reduces energy consumption but also minimizes damage to temperature-sensitive materials, making it promising for fabrication of solid-state batteries. A crucial challenge in cold sintering of solid electrolytes is achieving high ionic conductivity across grain boundaries. Exposure to the transient solvent can lead to incongruent dissolution, if elements dissolve to different degrees. Re-precipitation can then result in amorphous or secondary phases with disrupted composition and incomplete densification. Thus, incongruent dissolution often limits ionic conductivity of cold-sintered electrolytes.^[28] Co-sintering with polymers or lithium salts can help bypass these phases, and form continuous lithium-ion transport pathways, as shown in Figure 1.^[29]

We explored introducing polymer and lithium salt by varying the volume fraction of PPC-LiClO₄ in LLTO-polymer-salt composites (LLTO-PS), from 4%–13% by volume; these samples

are designated as LLTO-PS (4–13 vol%). The ionic conductivity of drop cast films of PPC-LiClO₄ is 7.8×10⁻⁵ S cm⁻¹ at room temperature (Figure S1, Supporting Information). We use 9 wt.% DMF as a sintering aid in the cold sintering process, which outperforms other solvents, such as acetone and dimethyl sulfoxide (DMSO), in promoting densification and optimizing interface design.^[21] Figure S2 shows the thermogravimetric analysis (TGA) of the cold sintered composite solid electrolyte. The weight loss (~1.7 wt.%) observed around 50 °C can be attributed to moisture trapped near the surface when the composite was exposed to air during sample preparation. PPC likely contributes to weight loss above 230 °C (~1.3 wt.%).^[30] We thus estimate the DMF residue in the composite solid electrolyte to be around 3–4 wt.%, which could enhance ionic conductivity.^[21]

We compare our cold sintered LLTO composites to LLTO cold sintered without PPC or LiClO₄ (using 9 wt.% DMF as the transient solvent, LLTO-PS (0 vol%)), and to LLTO cold sintered in air using deionized water as the transient solvent as previously reported for oxide electrolytes,^[14,20] again without adding polymer or lithium salt (CS LLTO). We also compare to LLTO densified at 1200 °C using conventional high-temperature sintering (HTS LLTO). Figure 2a and Table S1 (Supporting Information) show the density and relative density of cold-sintered composites and how they vary with composition. The density of composites decreases from 4.07 g/cm³ to 3.69 g/cm³, with the highest densification with 4% by volume of PPC-LiClO₄; the addition of polymer and salt appears to assist with densification when compared to neat LLTO, although at high polymer content densification decreases. HTS LLTO achieves

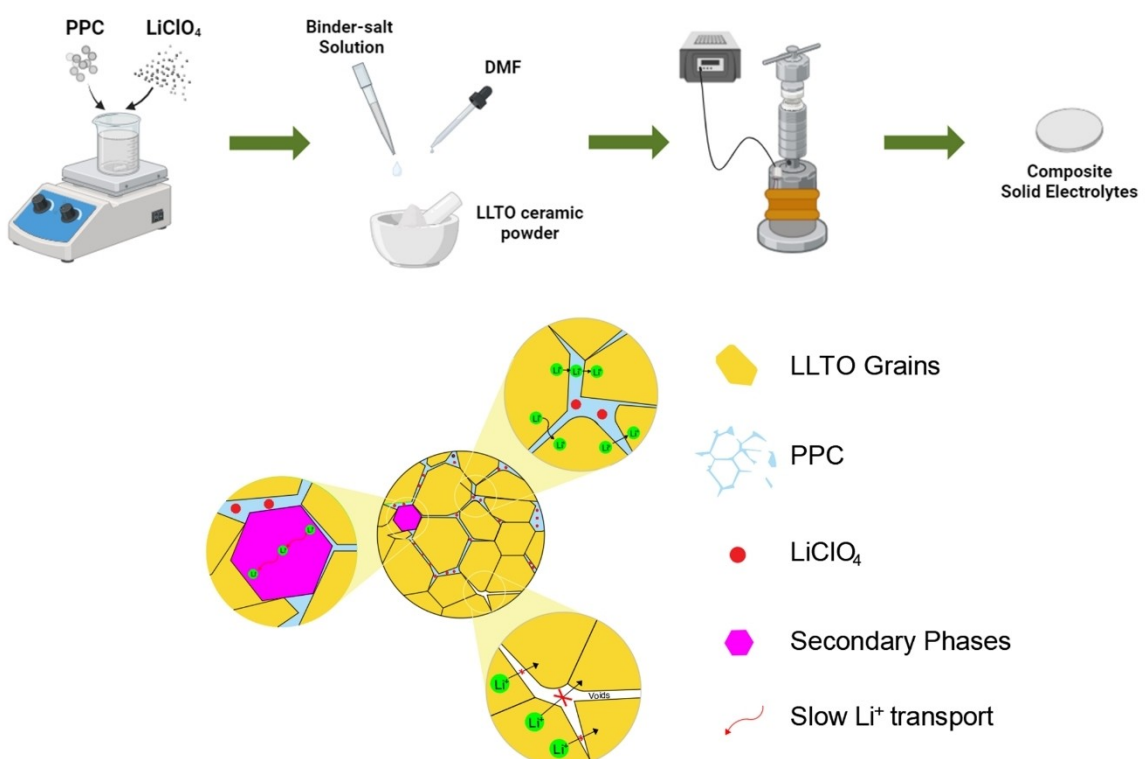


Figure 1. Schematic representation of cold sintering of LLTO solid electrolytes at 125 °C.

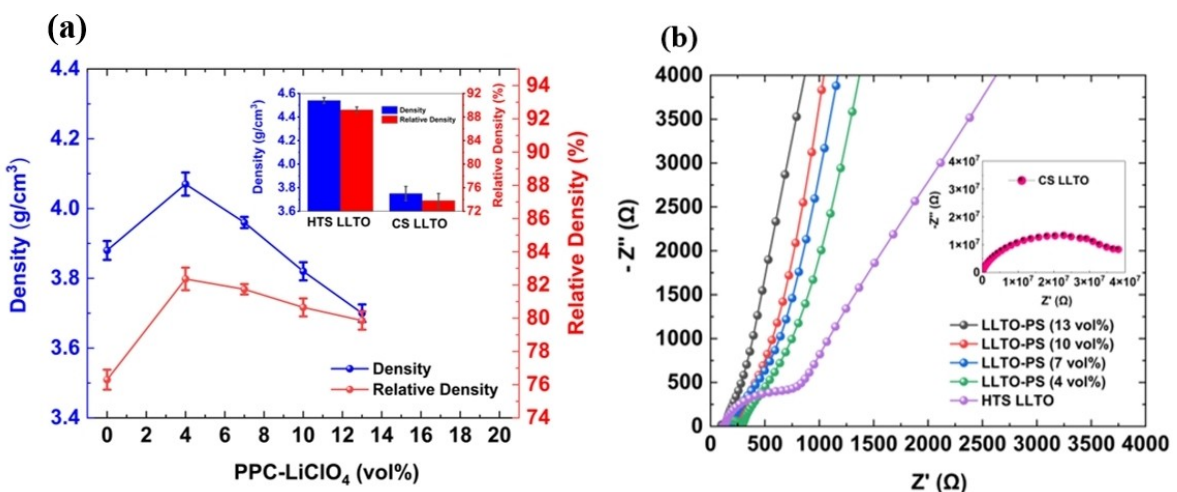


Figure 2. a) Density and relative density of composites as a function of volume percentage of PPC- LiClO_4 , and b) Nyquist plots of CS LLTO, LLTO-PS (4–13 vol %), and HTS LLTO solid electrolytes.

the highest density at $4.54 \text{ g}/\text{cm}^3$, and relative density at 89.2 %. LLTO cold sintered with 20 wt.% deionized water has the lowest relative density, approximately 74 % (CS LLTO).

Figure 2b shows the electrochemical impedance spectra of LLTO-PS (4–13 vol%), CS LLTO, and HTS LLTO. The equivalent circuit used to fit the complex impedance spectra of HTS LLTO consists of $(R_{\text{bulk}} \parallel | \text{CPE}_{\text{bulk}} \parallel (R_{\text{gb}} \parallel | \text{CPE}_{\text{gb}}) \text{-CPE}_{\text{tail}}$, where R and CPE denote the resistance and constant phase element, respectively. A parallel combination of a resistor (R_{bulk}) and a constant phase element (CPE_{bulk}), denoted as $R_{\text{bulk}} \parallel | \text{CPE}_{\text{bulk}}$, was employed to represent the bulk lithium-ion conductivity in LLTO. In addition, a parallel arrangement of a resistor R_{gb} and constant phase element CPE_{gb} , expressed as $R_{\text{gb}} \parallel | \text{CPE}_{\text{gb}}$, was used to characterize the lithium-ion conductivity at grain boundaries. The tail at the low-frequency region was represented by incorporating an additional constant phase element (CPE_{tail}) in series with the other circuit elements, as described previously, to model lithium-ion blocking electrodes (Figure S3, Supporting Information).^[31] The high-frequency semicircle from HTS-LLTO, associated with a capacitance of $3 \times 10^{-11} \text{ F}$, can be attributed to ion transport in the bulk. In contrast, the medium-frequency semicircle exhibits a capacitance of $2.93 \times 10^{-7} \text{ F}$, which we attribute to ion transport at the grain boundaries. In our cold sintered composite samples, the equivalent circuit is slightly different; the capacitances linked to the high-frequency and medium-frequency semicircles are on the order of 10^{-8} F and 10^{-6} F , respectively, both corresponding to ion transport across the grain boundaries. The increase in PPC- LiClO_4 content correlates with a decrease in grain boundary resistances.

Cold sintered composite solid electrolytes, incorporating 4–13 vol % PPC- LiClO_4 additives, demonstrate low total resistances. The total resistance exhibits a reduction from 810Ω (4 vol % PPC- LiClO_4) to 308Ω (13 vol % PPC- LiClO_4), correlating with the rise in polymer-lithium salt content. Bulk and grain boundary conductivity values for LLTO-PS (0–13 vol %) are tabulated (Table S2, Supporting Information). All composite samples exhibit similar bulk conductivities of about

$1 \times 10^{-3} \text{ S cm}^{-1}$, aligning with previously reported values for bulk lithium-ion conduction in LLTO.^[32] The grain boundary conductivity increases from $1.04 \times 10^{-4} \text{ S cm}^{-1}$ to $4.38 \times 10^{-4} \text{ S cm}^{-1}$ as the volume percentage of PPC- LiClO_4 increases from 4%–13%.

Figure 3a compares the total ionic conductivities of cold-sintered composite electrolytes, which incorporate varying content of PPC- LiClO_4 , with the total ionic conductivity of HTS LLTO. Conductivities are obtained from Nyquist plots of symmetric cells (Al/LLTO-PS (4–13 vol %)/Al and Ag/HTS LLTO/Ag) at room temperature. Changing the volume percentage of PPC- LiClO_4 in the composite solid electrolyte from 4%–13% significantly enhances ionic conductivity, increasing from $9.43 \times 10^{-5} \text{ S cm}^{-1}$ to $3.08 \times 10^{-4} \text{ S cm}^{-1}$. The Nyquist plot of LLTO-PS (0 vol %) is shown in Figure S4, and this sample exhibits low ionic conductivity, approximately $3 \times 10^{-11} \text{ S cm}^{-1}$. Similarly, using 20 wt.% deionized water as a transient solvent (CS LLTO) yields an exceptionally high resistance on the order of $10^7 \Omega$. The ionic conductivity of CS LLTO is low, near $6 \times 10^{-9} \text{ S cm}^{-1}$. The limited grain growth, porosity, and poor contact between grains, induced by the low-temperature sintering process, lead to poor ionic conductivity in the absence of binder-salt ionic pathways.^[33] As Figure 3a shows, HTS LLTO has an ionic conductivity of $1.34 \times 10^{-4} \text{ S cm}^{-1}$.

Although the ionic conductivity increases with PPC- LiClO_4 content, mechanical properties start degrading below 80 % relative density, and samples with greater than 13 % PPC- LiClO_4 content tend to fracture easily. The inset of Figure 3a shows the ionic conductivities reported for oxide-based electrolytes fabricated by cold sintering. The ionic conductivity of the cold-sintered composite $\text{Li}_{0.29}\text{La}_{0.57}\text{TiO}_3$ electrolyte remains below that of the composite $\text{Li}_{6.95}\text{Mg}_{0.15}\text{La}_{2.75}\text{Sr}_{0.25}\text{Zr}_2\text{O}_{12}$ electrolyte, such that LLTO exhibits the second highest conductivity among oxide-based solid electrolytes fabricated using the same sintering technique.

Figure 3b shows the temperature dependence of ionic conductivity of cold-sintered composite oxide solid electrolytes. The temperature dependence appears Arrhenius for all cold

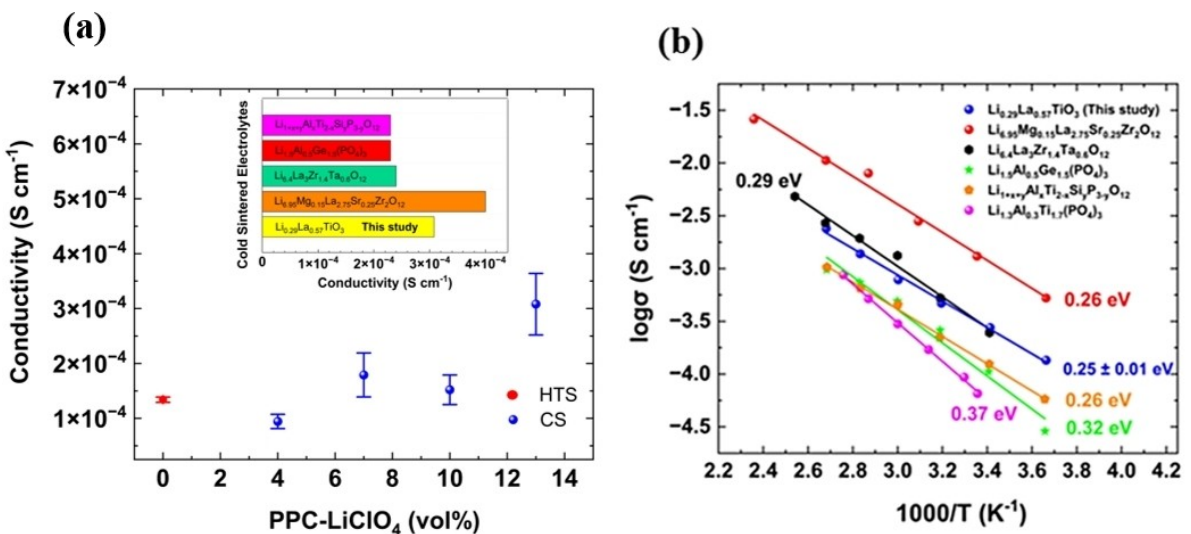


Figure 3. a) Ionic conductivity of LLTO-PS (4–13 vol%) and HTS LLTO at room temperature and comparison of the ionic conductivity of the cold sintered composite oxide solid electrolytes, and b) Arrhenius plots of our cold sintered composite electrolyte (LLTO-PS(13 vol%)) compared with other oxide solid electrolytes: Li_{1-x}Al_xGe_{1-y}PO₄,^[14] Li_{1+x+y}Al_xTi_{2-x}Si_yP_{3-y}O₁₂,^[14] Li_{1.3}Al_{0.3}Ti_{1.7}(PO₄)₃,^[20] Li_{0.95}Mg_{0.15}La_{0.25}Sr_{0.25}Zr₂O₁₂,^[21] Li_{0.4}La₃Zr_{1.4}Ta_{0.6}O₁₂,^[22]

sintered oxide composites, and activation energies fall within the range of 0.25 eV to 0.37 eV. LLTO composite electrolytes exhibit high ionic conductivities within the temperature range of 0–100 °C, exceeding all previously reported materials except Li_{0.95}Mg_{0.15}La_{0.25}Sr_{0.25}Zr₂O₁₂. The activation energy is also at the low end of the range, at 0.25 eV, which is consistent with previous reports of LLTO activation energies (0.3–0.4 eV).^[34] Incorporating an appropriate amount of PPC-LiClO₄ into the

perovskite LLTO can substantially enhance lithium-ion transport, leading to a decrease in the activation energy.

LLTO-PS (13 vol %) exhibits the highest ionic conductivity and a relative density of around 80%; therefore, we selected this sample for further characterization. Figure 4 displays the XRD patterns of the pristine LLTO powder and LLTO-PS (13 vol%). By comparing to reported data from LLTO (01-090-2573), we observe that both the cold-sintered composite solid

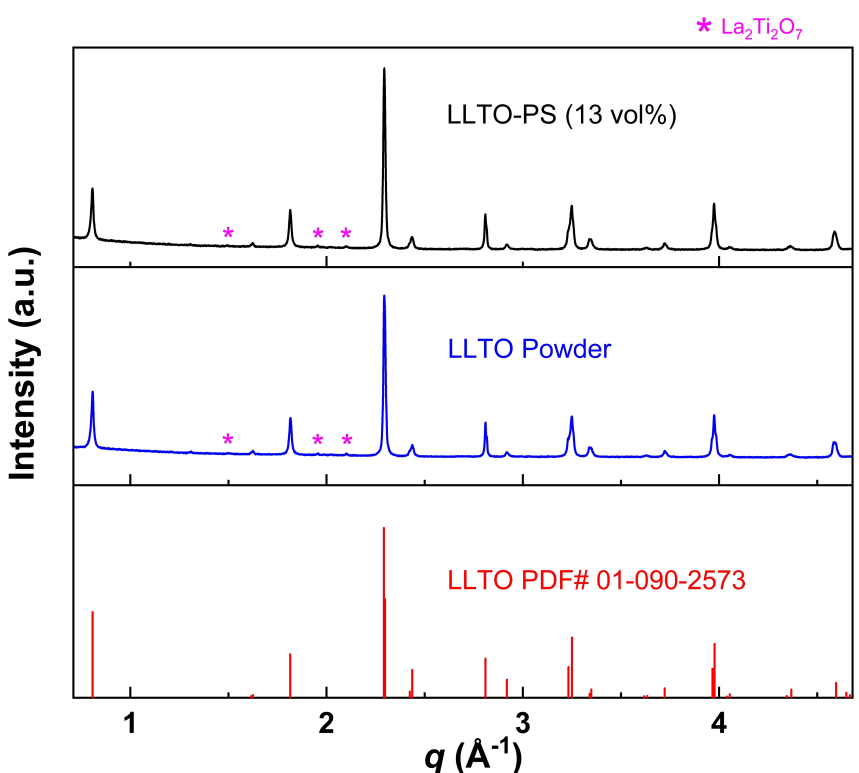


Figure 4. XRD patterns of LLTO powder and LLTO-PS (13 vol%).

electrolyte and the pristine powder exhibit a perovskite-type tetragonal crystal structure and a high degree of crystallinity. The sole impurity phase in the pristine LLTO powder is $\text{La}_2\text{Ti}_2\text{O}_7$ (04-021-8682), and is present in small amounts, approximately 2 wt%. Similarly, $\text{La}_2\text{Ti}_2\text{O}_7$ is the sole impurity phase observed in the cold-sintered solid electrolyte, with no change in its weight percentage. We therefore attribute the impurities in our composites to originate from the pristine LLTO powder rather than the cold sintering process. The crystal structure of the LLTO ceramic phase remains unchanged with the addition of PPC and LiClO_4 after cold sintering. Moreover, we speculate that the lack of secondary phase formation after the cold sintering process indicates congruent dissolution during exposure to the transient solvent.

Figure 5 shows SEM images capturing the fracture cross sections of the cold-sintered and conventionally sintered solid electrolytes, along with an image of the commercial-grade LLTO powder. The cross-sectional images were acquired without polishing; a 5 nm-thick iridium layer was sputtered onto the fractured surfaces to prevent charging. The powder has an average particle size of 1–2 μm . High-temperature sintering conducted at 1200 °C for 10 hours substantially increases the average grain size, reaching 5 μm . This microstructure is distinguished by the establishment of intimate inter-grain contact within the ceramic structure, accompanied by a reduction in porosity. Atomic diffusion is substantial at elevated temperatures, and ultimately leads to a densely packed structure.

Figure 5c shows the microstructure of the cold-sintered composite electrolyte that incorporates 13 vol% of PPC- LiClO_4 . The composite solid electrolyte, post-cold sintering at 125 °C, exhibits an average grain size of approximately 1–2 μm , mirroring the initial particle size of the powder. This consistency indicates the absence of discernible grain growth due to cold sintering of LLTO. CS LLTO demonstrates a microstructure similar to the cold-sintered composite sample, with no apparent grain growth. Despite the composite sample having a lower density than the conventionally sintered solid electrolyte, introducing a binder-salt solution effectively establishes conductive pathways by filling the voids between ceramic grains. This leads to high ionic conductivities in the composite samples despite sintering at temperatures approximately 1000 °C lower than those processed through high-temperature sintering.

The direct contact between lithium metal and our LLTO solid electrolyte induces the reduction of Ti^{4+} to lower oxidation states. As a result, the electronic conductivity of the solid electrolyte increases, ultimately leading to battery self-discharge.^[35] To prevent the reduction of Ti^{4+} within LLTO by Li metal and to reduce interfacial resistance, we incorporated a 4 M lithium bis(fluorosulfonyl)imide (LiFSI) solution in dimethoxyethane (DME) ($\approx 5 \mu\text{L}\text{cm}^{-2}$) at the Li/LLTO interface. Nevertheless, the Li/LLTO-PS (13 vol%)/LFP cell voltage rapidly declines to nearly 0 V even before galvanostatic charge and discharge tests. A Li/LLTO-PS (13 vol%)/Li symmetric cell was assembled by introducing a trace amount of solution at the interfaces. The cell was subjected to a current density of 0.2 mAcm^{-2} for a few hours before being disassembled to

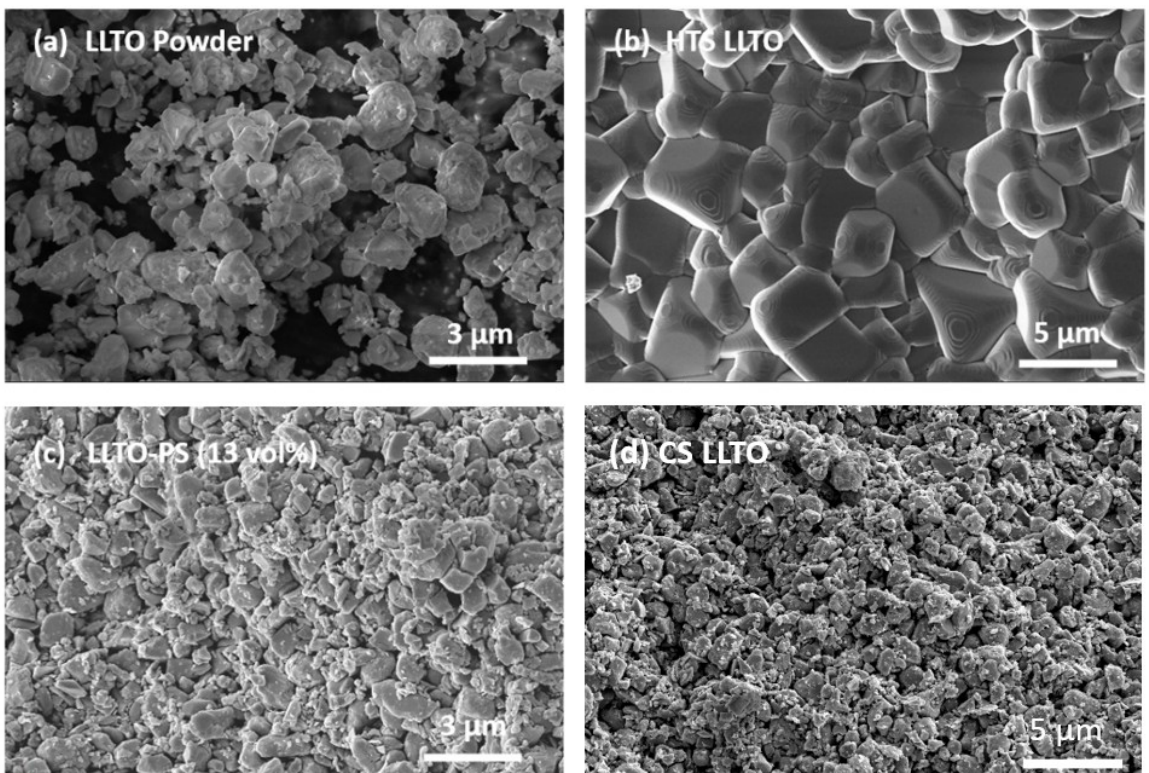


Figure 5. SEM images of a) LLTO powder, b) HTS LLTO, c) LLTO-PS (13 vol%), and d) CS LLTO.

measure the electronic conductivity of the LLTO solid electrolyte. The electronic conductivity of the LLTO solid electrolyte was less than $2 \times 10^{-9} \text{ S cm}^{-1}$ before contact with Li metal. After disassembly, the electronic conductivity of the LLTO solid electrolyte increases to approximately $6 \times 10^{-5} \text{ S cm}^{-1}$, and the color of the solid electrolyte turned from white to black.

To evaluate the evolution of interfacial resistance, we performed time-resolved impedance spectroscopy experiments.^[36] We fabricated symmetric cells, Li/LLTO-PS (13 vol %)/Li, and show Nyquist plots of cells at 30 min, 5 h, 30 h, and 54 h after cell assembly in Figure S5a. The evolution of interfacial resistance and total resistance of the symmetric cell is shown in Figure S5b. The measurements were taken from 30 minutes to 54 hours after cell assembly. The interfacial impedance steadily increases over time, exhibiting a sharp rise from $1087 \Omega \text{cm}^2$ to $10,690 \Omega \text{cm}^2$, with no indication of stabilization. This suggests the formation of a steadily growing interphase between lithium metal and LLTO composite solid electrolytes. After time-resolved impedance measurements, the symmetric cell was disassembled, revealing significant degradation in the solid electrolyte. This degradation was characterized by a color change, with the appearance of dark and gray regions, along with a yellow hue at the interface (Figure S5e, Supporting Information).

We also added a PVDF membrane soaked in a liquid electrolyte (LiPF_6 , 1 M in ethylene carbonate and dimethyl carbonate) as an interfacial layer between the Li anode and the solid electrolyte. When PVDF is employed, the electrical conductivity of the solid electrolyte remains unaffected. A similar approach was used to prevent the reduction of Ti^{4+} in LLTO when in contact with lithium metal by adding a PEO layer at the LLTO/Li interface.^[37] This strategy effectively inhibits electron conduction across the solid electrolyte, thus minimizing the risk of failure. Figure S5c shows the Nyquist plot of the Li/PVDF/LLTO-PS (13 vol %)/PVDF/Li cell at 30 min, 4 h, 25 h, and 72 h after cell assembly. The evolution of the interfacial resistance and total resistance of the symmetric cell with PVDF layers is shown in Figure S5d. The interfacial impedance of the cell stabilizes after approximately 20 hours and remains unchanged at around $1170 \Omega \text{cm}^2$, even after more than 72 hours. We speculate that interfacial reactions are complete approximately 20 hours after cell assembly, such that any interphases that formed do not grow further. The inclusion of PVDF soaked with liquid electrolyte in the symmetric cell promotes the formation of a stable interphase, and effectively prevents the degradation of LLTO solid electrolytes.

The electrochemical performance of LLTO-PS (13 vol %) was evaluated in symmetric Li metal cells (Li/PVDF/LLTO-PS (13 vol %)/PVDF/Li) to investigate the stability of the solid electrolyte and its ability to suppress lithium dendrite growth. The applied current density was incrementally increased to determine the critical current density (CCD) of the cell, beginning at 0.1 mA cm^{-2} , with a fixed Li plating/stripping duration of 1 hour. We take the CCD to be the highest current density that the solid-state electrolyte can withstand without experiencing short circuits due to Li-dendrite penetration.^[38] As shown in Figure 6a, the symmetric cell exhibits stable cycling

under various current densities, while a sharp voltage increase was observed at a current density of 2 mA cm^{-2} . The Li/PVDF/LLTO-PS (13 vol %)/PVDF/Li cell demonstrates a high CCD exceeding 1.8 mA cm^{-2} , surpassing values previously reported for cells with various oxide-based ceramic electrolytes, as illustrated in Figure S6 (Supporting Information).

We also measured the critical current density of symmetric cells with PVDF and PPC-LiClO₄ as the separator, Li/PVDF/PPC-LiClO₄/PVDF/Li, with PVDF soaked in the same amount of liquid electrolyte as when used at interfaces in LLTO-based symmetric cells. The Li/PVDF/PPC-LiClO₄/PVDF/Li cell exhibits a CCD of 2.6 mA cm^{-2} , slightly higher, but overall similar, than that of the LLTO-PS (13 vol %) symmetric cells (Figure S7a, Supporting Information).

Long-term galvanostatic stripping and plating tests were performed at various current densities to assess the stability of the symmetric cell. Figure 6b shows the galvanostatic cycling voltage profiles of the Li/PVDF/LLTO-PS (13 vol %)/PVDF/Li cell at varying current densities. The cell shows good cycling performance, maintaining stability for over 400 hours with low polarization overpotentials of approximately 80 mV, 120 mV, and 140 mV at current densities of 0.1 mA cm^{-2} , 0.2 mA cm^{-2} , and 0.3 mA cm^{-2} , respectively. The initial voltage of 200 mV decreased to 80 mV after 24 hours of cycling, and the cell maintained stable cycling at this voltage until the current density was raised to 0.2 mA cm^{-2} . We attribute this behavior to the formation and stabilization of the solid electrolyte interphase (SEI) layer, as LiPF_6 , ethylene carbonate (EC), and dimethyl carbonate (DMC) contribute to the formation of an SEI layer when exposed to lithium metal anodes.^[39] When the current density is reduced from 0.3 mA cm^{-2} to 0.1 mA cm^{-2} , the polarization decreases to approximately 50 mV, substantially less than the initial polarization at 0.1 mA cm^{-2} .

To investigate the cause of the reduction in polarization, we show the cycling performance of the Li/PVDF/PPC-LiClO₄/PVDF/Li cell at varying current densities of 0.1 mA cm^{-2} , 0.2 mA cm^{-2} , and 0.3 mA cm^{-2} in Figure S7b. The cycling behavior of the cell is similar to that of the symmetric cell with LLTO-PS; a decrease in polarization is observed both after the initial cycling at 0.1 mA cm^{-2} and when the current density switches back to 0.1 mA cm^{-2} after cycling at 0.3 mA cm^{-2} . This indicates that the decrease in voltage after cycling at 0.3 mA cm^{-2} is driven by changes to our interfacial layers rather than by the degradation of the LLTO-PS solid electrolyte. We anticipate that increasing current densities may induce changes at the interface, enhancing the contact area and facilitating ionic conduction, lowering impedance. Furthermore, cycling could alter the morphology of the SEI, potentially further affecting interfacial resistances. The voltage of the symmetric Li/PVDF/LLTO-PS (13 vol %)/PVDF/Li cell remains unchanged when the current density is switched back to 0.1 mA cm^{-2} for the third time, in contrast to the decrease observed during the second cycle at the same current density, indicating the stabilization of the interface. In addition, the cell was disassembled after the cycling test, and no color change was observed in the cold-sintered composite electrolyte (Figure S7c, Supporting Information). The detailed voltage profile at a current density of 0.3 mA cm^{-2} is shown in Figure 6c.

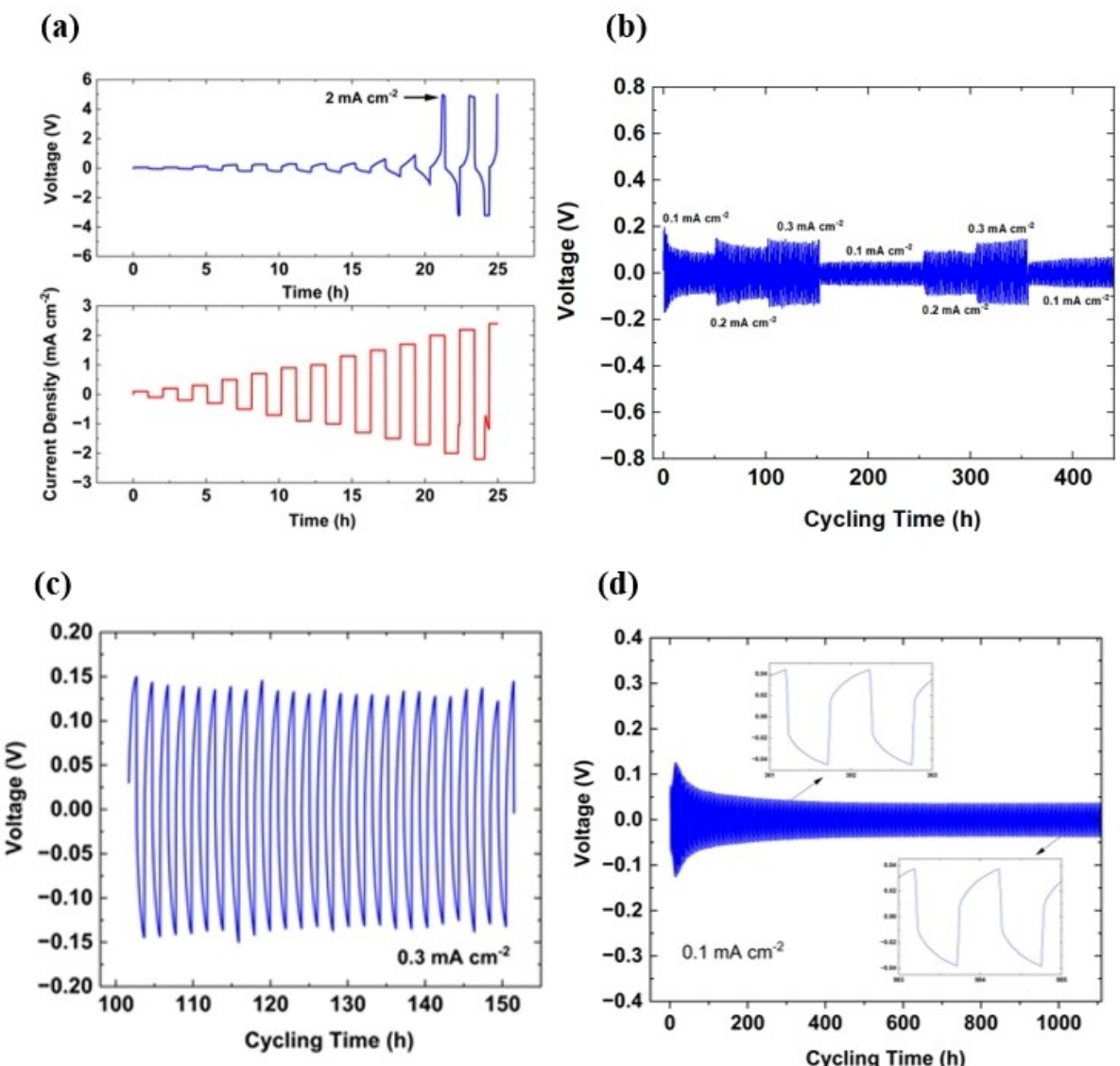


Figure 6. a) Critical current density test of the Li/PVDF/LLTO-PS (13 vol%)/PVDF/Li cell by galvanostatic cycling. b) Cycling performance of a Li/PVDF/LLTO-PS (13 vol%)/PVDF/Li cell under different current densities. c) voltage profile at 0.3 mA cm^{-2} , and d) Cycling performance of the Li/PVDF/LLTO-PS (13 vol%)/PVDF/Li cell at 0.1 mA cm^{-2} .

Figure 6d illustrates the cycling performance of the Li/PVDF/LLTO-PS (13 vol%)/PVDF/Li cell at 0.1 mA cm^{-2} . The cell demonstrates excellent cycling stability at this current density for over 1000 hours.

A solid-state Li/LFP cell was fabricated using LLTO-PS (13 vol%) as a solid electrolyte. The cold sintering process enables the co-sintering of solid electrolyte and cathode materials, promoting intimate physical contact and minimizing interfacial resistance. Cold sintering also avoids elemental mixing across the interface, thereby retaining the integrity of the assembled components.^[18] We co-sintered LLTO solid electrolytes and LFP electrodes at 400 MPa and 125 °C for 30 minutes. Reducing the composite pellet thickness to ~0.4 mm in the full cell configuration allows for lower sintering pressure and a shorter sintering duration. The properties of the composite solid electrolyte used in full cell fabrication are listed

in Table S3, and the Nyquist plot of the electrolyte is shown in Figure S8. The electrolyte exhibits an ionic conductivity of $2.86 \times 10^{-4} \text{ Scm}^{-1}$ and a relative density of 79.2%. Figure S9 shows the cross-sectional SEM image of the co-sintered LFP cathode and solid electrolyte, along with the corresponding EDS elemental map. Cold sintering leads to intimate contact between the cathode and electrolyte layers. We add an electrolyte solution-soaked PVDF membrane between the solid electrolyte and lithium foil to assemble the full device within a 2032 coin cell, as illustrated in Figure 7a.

Figure 7b shows the Nyquist plot of the Li/PVDF/LLTO-PS (13 vol%)/LFP cell at room temperature. The electrochemical impedance spectrum exhibits distinct semicircles at high and mid-frequencies, along with a low-frequency tail (Figure S10, Supporting Information). We attribute R_1 and R_2 to the solid electrolyte resistance, and R_3 to interfacial resistance, with a

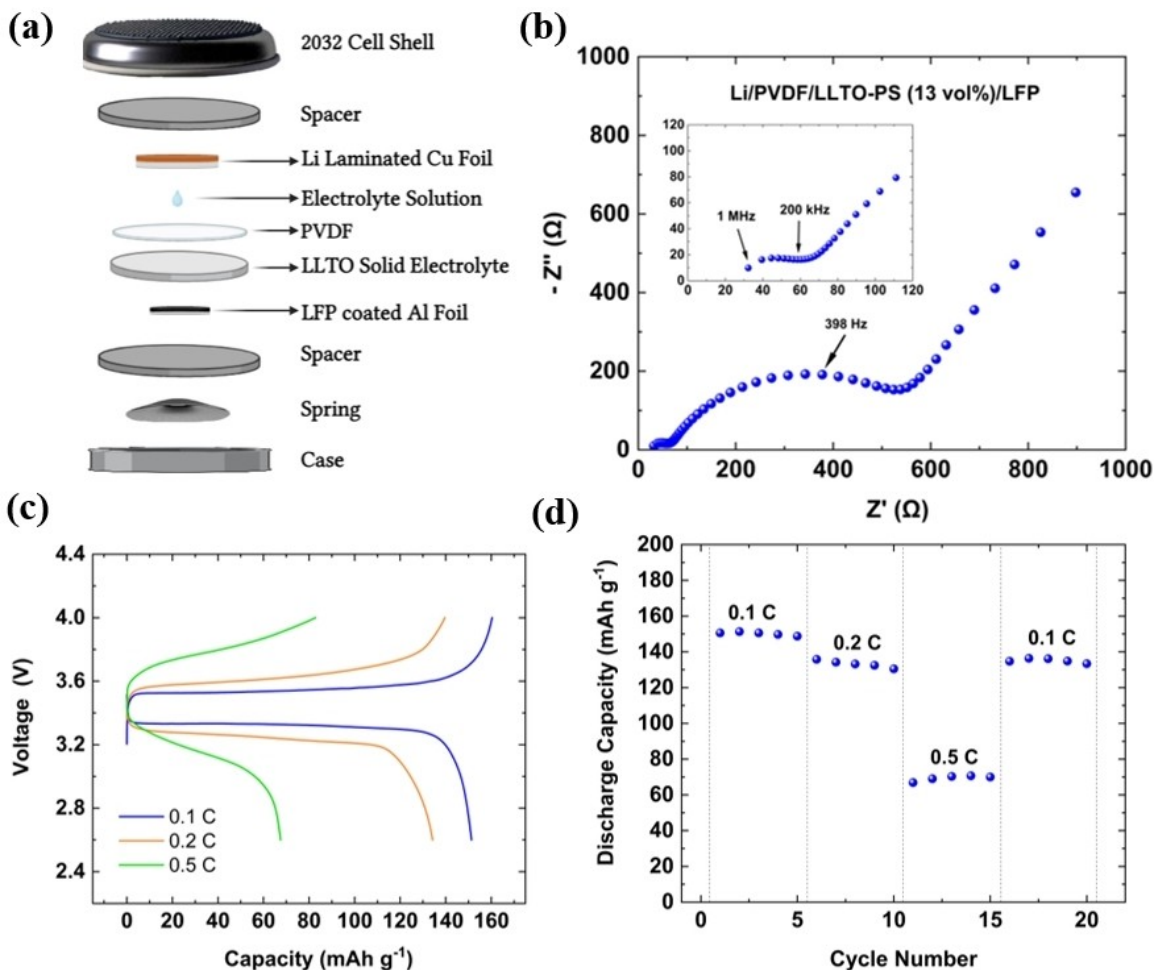


Figure 7. a) Schematic illustration of the components of our batteries. b) Nyquist plot (inset: data at high frequency). c) Galvanostatic charge/discharge curves, and d) rate performance of a Li/PVDF/LLTO-PS (13 vol %)/LFP cell at room temperature.

capacitance of $6.39 \times 10^{-6} \text{ F}$.^[40] The solid electrolyte resistance is estimated to be 330Ω , while the interfacial resistance is approximately 215Ω . Figure 7c shows the voltage profiles of the full cell at various current densities. The full cell exhibits a discharge capacity of 151 mAh g^{-1} at 0.1 C and shows a typical voltage profile of Li/LFP, featuring a flat plateau at $\sim 3.45 \text{ V}$ during galvanostatic charging and discharging. In addition, the rate performance of the cell at 0.1 , 0.2 , and 0.5 C is shown in Figure 7d. The full cell exhibits a maximum discharge capacity of 135 mAh g^{-1} at 0.2 C and 70 mAh g^{-1} at 0.5 C , respectively. The cell demonstrated a near-steady discharge capacity profile at 0.1 , 0.2 , and 0.5 C .

The cycling stability of the Li/PVDF/LLTO-PS (13 vol %)/LFP cell at room temperature, tested at 0.1 C , 0.2 C , and 0.5 C for 30 cycles, is shown in Figure S11. The cell exhibits modest cycling performance, retaining 71.3% of its initial capacity after 30 cycles, with a discharge capacity of 113 mAh g^{-1} at 0.1 C . Similarly, the cell achieves a capacity retention rate of 69.1%, with a discharge capacity of 92 mAh g^{-1} after 30 cycles at 0.2 C . At 0.5 C , the capacity decay becomes increasingly pronounced, leading to a capacity retention rate of 46.7% after 30 cycles, with a discharge capacity of 59 mAh g^{-1} . The pronounced

capacity decay observed at 0.5 C may result from multiple degradation mechanisms, including lithium dendrite formation, LiPF_6 decomposition, and PVDF membrane deterioration under high C-rate conditions.

3. Conclusions

We fabricated perovskite composite solid electrolytes by integrating PPC- LiClO_4 into a main LLTO ceramic phase through a low-temperature sintering process at 125°C , using DMF as the transient liquid phase. We explored the effect of varying volume fractions of PPC- LiClO_4 on the relative density and ionic conductivity of the composite electrolytes. Cold sintering of LLTO at 125°C with PPC- LiClO_4 leads to a high ionic conductivity of $3 \times 10^{-4} \text{ S cm}^{-1}$ at room temperature, comparable to that of LLTO conventionally sintered at 1200°C . The ionic conductivity values between 0 and 100°C show a low activation energy of 0.25 eV . The symmetric Li/LLTO-PPC- LiClO_4 /Li cell with PVDF interlayers achieves a high critical current density of 1.8 mA cm^{-2} at room temperature and demonstrates good cycling performance, maintaining stability for over 400 hours

with low polarization overpotentials at different current densities. Solid-state lithium batteries fabricated with LLTO composite solid electrolytes deliver a high discharge capacity of 151 mAh g^{-1} at 0.1 C and 135 mAh g^{-1} at 0.2 C. Altogether, cold sintering represents a promising method for producing composite solid electrolytes by co-sintering ceramic and polymer materials.

Materials and Methods

Cold Sintering of LLTO Composite Solid Electrolytes

A binder-salt solution was prepared with a 2:1 molar ratio of PPC to LiClO_4 . $\text{Li}_{0.29}\text{La}_{0.57}\text{TiO}_3$ powders, designated as TP-02F with a particle size distribution (D50) of less than 1 μm , were purchased from Toho Titanium Co., Ltd. PPC and LiClO_4 were purchased from Sigma-Aldrich. In the preparation of the binder-salt solution, the binder and lithium salt were dissolved in acetonitrile. The resulting mixture was stirred overnight at 25°C using a magnetic stirrer. Afterward, the LLTO powder was mixed with the binder-salt solution and DMF. Subsequently, the mixture was mixed using an agate mortar and pestle for 5 minutes.

To explore the influence of introducing polymer-lithium salt on lithium-ion conductivity and relative density, the volume fractions of PPC- LiClO_4 were systematically varied with respect to the LLTO-polymer-salt composite (LLTO-PS), ranging from 0%–13% by volume (designated as LLTO-PS (0–13 vol%). 9 wt.% DMF was used as the cold sintering solvent. The resulting wetted powder was placed in a 13 mm die and sandwiched between aluminum foils, serving as blocking electrodes for impedance measurements. The die was then surrounded by a jacket connected to a heating element, equipped with a thermocouple, and loaded into a uniaxial press to apply pressure and heat simultaneously. The composite powder was subjected to uniaxial pressure of 600 MPa at 125°C for 1 h with a ramp-up rate of $10^\circ\text{C}/\text{minute}$. Next, the composite sample with a thickness of around 1 mm was assembled within a 2032 coin cell to conduct electrochemical impedance spectroscopy (EIS) measurements. Both the preparation of the binder-salt solution and the cold sintering process of the composite powder were performed in an Ar-filled glove box.

Another sample was produced in air using deionized water as the transient solvent without adding polymer and lithium salt to investigate the effect of a binder-salt solution between ceramic grains (designated as CS LLTO). 20 wt.% of deionized water was added to LLTO powder and mixed in a mortar and pestle for 5 minutes. Next, the powder was subjected to uniaxial pressure of 600 MPa at 125°C for 2 hours at a ramp-up rate of $10^\circ\text{C}/\text{minute}$, and the solid electrolyte was assembled within a 2032 coin cell for EIS measurements. In addition, a sample was fabricated for comparative analysis using the conventional high-temperature sintering technique (designated as HTS LLTO). To fabricate LLTO solid electrolytes measuring 12.7 mm in diameter and 1 mm in thickness, a uniaxial force of 75 kN was applied to the powder for 5 minutes. In the subsequent step, the samples were buried in LLTO powder within an alumina crucible to mitigate the potential loss of lithium. The sintering step was performed at 1200°C for 10 hours with ramp-up and ramp-down rates of 5°C per minute.

Characterization and Measurement

The relative density of the sintered LLTO solid electrolytes was determined by measuring the mass and volume of the pellets,

followed by the calculation of their density and comparison to the theoretical density of LLTO ($\rho_{\text{LLTO}} = 5.09 \text{ g cm}^{-3}$). In addition, the relative density of the composite solid electrolytes was calculated by determining the ratio of the measured densities to the theoretical density of the composite, which comprises the ceramic LLTO phase, PPC ($\rho_{\text{PPC}} = 1.26 \text{ g cm}^{-3}$), and LiClO_4 ($\rho_{\text{LiClO}_4} = 2.42 \text{ g cm}^{-3}$). The theoretical density of the composite solid electrolytes can be calculated using the following equation:^[41]

$$\rho_{\text{composite}} = \rho_{\text{LLTO}} f_{\text{LLTO}} + \rho_{\text{PPC}} f_{\text{PPC}} + \rho_{\text{LiClO}_4} f_{\text{LiClO}_4} \quad (1)$$

where ρ_{LLTO} , ρ_{PPC} , and ρ_{LiClO_4} represent the density of LLTO, PPC, and LiClO_4 , respectively, while f_{LLTO} , f_{PPC} , and f_{LiClO_4} are the volume fraction of LLTO, PPC, and LiClO_4 . The impedance spectra of the sintered solid electrolytes were acquired by EIS, with a 10 mV AC amplitude within the frequency range of $1\text{--}10^6 \text{ Hz}$ (Modulab XM, Solartron Analytical). Silver layers, each 100 nm thick, were sputtered onto both sides of the HTS LLTO solid electrolytes to serve as ion-blocking electrodes (Q150R, Quorum). ZView software was used from Scribner Associates (USA) to perform EIS data fitting through equivalent circuit modeling. The ionic conductivity (σ_{ion}) of the solid electrolytes is calculated using the following equation:^[42]

$$\sigma_{\text{ion}} = \frac{t}{R_{\text{total}} A} \quad (2)$$

where R_{total} and t represent the total resistance and thickness of the solid electrolyte, respectively, while A stands for the area of ion-blocking electrodes. The ionic conductivity of the samples was measured from $0\text{--}100^\circ\text{C}$ in 20°C intervals to elucidate the temperature dependence of the ionic conductivity of the samples. At each measurement point, the temperature was stabilized for 10 minutes. The activation energies of the sintered solid electrolytes were calculated from the slope of the Arrhenius plot using the following equation:

$$\sigma_{\text{ion}} = A \exp\left(-\frac{E_a}{k_B T}\right) \quad (3)$$

where A is the pre-exponential factor, E_a is the activation energy, k_B is the Boltzmann constant, and T is the absolute temperature.

Thermal analysis was conducted using a thermogravimetric analyzer (Q600 SDT, TA Instruments) to determine the amount of DMF residue in the cold-sintered composite solid electrolytes. The sample was heated from room temperature to 400°C at a rate of $10^\circ\text{C}/\text{min}$ in an inert nitrogen atmosphere, with the temperature equilibrated at 50°C for 10 minutes to remove moisture. Phase identification and crystal structure determination were conducted using an X-ray diffractometer (Empyrean, Malvern Panalytical). X-ray diffraction (XRD) patterns were obtained with $\text{Cu}-\text{K}\alpha$ radiation in the 2θ range of $10^\circ\text{--}70^\circ$, using a step size of 0.013° . The collected XRD patterns were analyzed using MDI Jade software. The microstructural analysis of the specimens was conducted on fractured surfaces using a Thermo Fisher Scientific Verios scanning electron microscope (SEM). Before SEM analysis, a thin iridium layer ($\sim 5 \text{ nm}$) was sputtered onto the fractured surfaces to prevent charging. Electronic conductivity measurements were performed through DC measurements, with two ion blocking electrodes made of silver layers that are 100 nm thick.

Fabrication of Li/LLTO/LFP Full Cells and Performance Testing

To demonstrate the practical functionality of LLTO-based electrolytes, solid-state lithium metal batteries were fabricated using cold-sintered LLTO-PPC-LiClO₄ composite electrolytes. An 8 mm punch was used to cut lithium discs from lithium foil (MSE Supplies, the thickness of lithium and copper is $\approx 40 \mu\text{m}$ and $11 \mu\text{m}$, respectively). LFP-based cathode sheets (MTI Corporation, the thickness of LFP and aluminum is $\approx 68 \mu\text{m}$ and $16 \mu\text{m}$, respectively) were dried in a vacuum oven at 100°C for 6 h and stored in an argon-filled glovebox to ensure the best performance. A 6 mm punch was used to cut LFP discs from the stored sheets. The as-prepared PPC-LiClO₄ solution was mixed with LLTO powder, followed by the addition of 9 wt.% DMF. The composite powder was then ground using an agate mortar and pestle for 5 minutes. Afterward, the wetted powder was placed into a 13 mm die, with a 6 mm LFP disc centered on top of it. The composite powder and LFP disc were co-sintered under a uniaxial pressure of 400 MPa at 125°C for 30 minutes. This process facilitates intimate contact between the $\sim 0.4 \text{ mm}$ thick solid electrolyte and the positive electrode. To prevent interfacial reactions between the lithium metal anode and LLTO-based composite solid electrolyte, an electrolyte solution-soaked ($\approx 20 \mu\text{L cm}^{-2}$ of LiPF₆, 1 M, EC/DMC (v/v ratio 50/50), Sigma-Aldrich, CA) PVDF membrane (0.45 μm , Amersham, Germany) was placed between the solid electrolyte and the anode. Next, the battery cell was assembled within a CR2032 coin cell, galvanostatically charged, and discharged between 2.6 V and 4.0 V vs. Li⁺/Li at room temperature using a battery testing device (BTS3000, Neware). The charging and discharging current densities were determined from the theoretical capacity of the LFP cathode, 170 mAh g^{-1} .

Acknowledgements

The authors acknowledge financial support from the U.S. National Science Foundation under Award Number 2134643. This material is based upon work supported in part by the U.S. Department of Defense, Army Research Laboratory, and Army Research Office under grant number W911NF-23-2-0229. A.K., G.V., and N.E. acknowledge support from the TUBITAK BIDEB 2214-A and 2211-C research programs under Project Codes 1059B142200202 and 1649B032200187, as well as the funding provided by Bogazici University BAP with grant number 19705D. The co-authors acknowledge use of the Penn State Materials Characterization Lab.

Conflict of Interests

The authors declare no conflict of interest.

Data Availability Statement

The data that support the findings of this study are available from the corresponding author upon reasonable request.

Keywords: Solid-state lithium batteries • Cold sintering process • Composite electrolytes • Lithium-ion conductivity • Lithium lanthanum titanate

- [1] a) M. A. Hannan, M. M. Hoque, A. Mohamed, A. Ayob, *Renew. Sustain. Energy Rev.* **2017**, *69*, 771; b) T. Kim, W. Song, D.-Y. Son, L. K. Ono, Y. Qi, *J. Mater. Chem. A* **2019**, *7*, 2942.
- [2] K. Xu, *Chem. Rev.* **2014**, *114*, 11503.
- [3] J. Janek, W. G. Zeier, *Nat. Energy* **2016**, *1*, 16141.
- [4] a) X.-B. Cheng, R. Zhang, C.-Z. Zhao, Q. Zhang, *Chem. Rev.* **2017**, *117*, 10403; b) M. Qi, L. Xie, Q. Han, L. Zhu, L. Chen, X. Cao, *J. Energy Storage* **2022**, *47*, 103641; c) W. Xu, J. Wang, F. Ding, X. Chen, E. Nasybulin, Y. Zhang, J.-G. Zhang, *Energy Environ. Sci.* **2014**, *7*, 513; d) Y. Zhang, T.-T. Zuo, J. Popovic, K. Lim, Y.-X. Yin, J. Maier, Y.-G. Guo, *Mater. Today* **2020**, *33*, 56.
- [5] a) S. Menkin, J. B. Fritzke, R. Larner, C. de Leeuw, Y. Choi, A. B. Gunnarsdóttir, C. P. Grey, *Faraday Discuss.* **2024**, *248*, 277; b) P. Bai, J. Li, F. R. Brushett, M. Z. Bazant, *Energy Environ. Sci.* **2016**, *9*, 3221; c) D. Cao, X. Sun, Q. Li, A. Natan, P. Xiang, H. Zhu, *Matter* **2020**, *3*, 57.
- [6] a) X. Wu, K. Song, X. Zhang, N. Hu, L. Li, W. Li, L. Zhang, H. Zhang, *Front. Energy Res.* **2019**, *7*, 65; b) M. F. Lagadec, R. Zahn, V. Wood, *Nat. Energy* **2019**, *4*, 16.
- [7] a) T. Mageto, S. D. Bhoyate, F. M. de Souza, K. Mensah-Darkwa, A. Kumar, R. K. Gupta, *J. Energy Storage* **2022**, *55*, 105688; b) A. Manthiram, X. Yu, S. Wang, *Nat. Rev. Mater.* **2017**, *2*, 16103.
- [8] a) Y.-K. Sun, *ACS Energy Lett.* **2020**, *5*, 3221; b) C. Li, Z.-Y. Wang, Z.-J. He, Y.-J. Li, J. Mao, K.-H. Dai, C. Yan, J.-C. Zheng, *Sustain. Mater. Technol.* **2021**, *29*, e00297; c) Y. Wu, S. Wang, H. Li, L. Chen, F. Wu, *InfoMat* **2021**, *3*, 827.
- [9] H. Aziam, B. Larhib, C. Hakim, N. Sabi, H. Ben Youcef, I. Saadoune, *Renew. Sustain. Energy Rev.* **2022**, *167*, 112694.
- [10] a) L. Long, S. Wang, M. Xiao, Y. Meng, *J. Mater. Chem. A* **2016**, *4*, 10038; b) Y. Zhao, L. Wang, Y. Zhou, Z. Liang, N. Tavajohi, B. Li, T. Li, *Adv. Sci.* **2021**, *8*, 2003675.
- [11] a) J. C. Bachman, S. Muy, A. Grimaud, H.-H. Chang, N. Pour, S. F. Lux, O. Paschos, F. Maglia, S. Lupart, P. Lamp, L. Giordano, Y. Shao-Horn, *Chem. Rev.* **2016**, *116*, 140; b) A. K. Mishra, H. A. Chaliyawala, R. Patel, S. Paneliya, A. Vanpariya, P. Patel, A. Ray, R. Pati, I. Mukhopadhyay, *J. Electrochem. Soc.* **2021**, *168*, 080536.
- [12] a) C.-A. Lin, M. Ihrig, K.-C. Kung, H.-C. Chen, W. S. Scheld, R. Ye, M. Finsterbusch, O. Guillou, S.-K. Lin, *J. Eur. Ceram. Soc.* **2023**, *43*, 7543; b) M. V. Reddy, C. M. Julien, A. Mauger, K. Zaghib, *Nanomaterials* DOI: 10.3390/nano08081606.
- [13] a) K. J. Kim, M. Balaish, M. Wadaguchi, L. Kong, J. L. M. Rupp, *Adv. Energy Mater.* **2021**, *11*, 2002689; b) E. Rangasamy, J. Wolfenstine, J. Sakamoto, *Solid State Ion.* **2012**, *206*, 28; c) Y. Liu, Q. Sun, D. Wang, K. Adair, J. Liang, X. Sun, *J. Power Sources* **2018**, *393*, 193.
- [14] W. Lee, C. K. Lyon, J.-H. Seo, R. Lopez-Hallman, Y. Leng, C.-Y. Wang, M. A. Hickner, C. A. Randall, E. D. Gomez, *Adv. Funct. Mater.* **2019**, *29*, 1807872.
- [15] a) G. Vardar, W. J. Bowman, Q. Lu, J. Wang, R. J. Chater, A. Aguadero, R. Seibert, J. Terry, A. Hunt, I. Waluyo, D. D. Fong, A. Jarry, E. J. Crumlin, S. L. Hellstrom, Y.-M. Chiang, B. Yildiz, *Chem. Mater.* **2018**, *30*, 6259; b) Y. Kim, D. Kim, R. Bliem, G. Vardar, I. Waluyo, A. Hunt, J. T. Wright, J. P. Katsoudas, B. Yildiz, *Chem. Mater.* **2020**, *32*, 9531.
- [16] J. Guo, A. L. Baker, H. Guo, M. Lanagan, C. A. Randall, *J. Am. Ceram. Soc.* **2017**, *100*, 669.
- [17] a) H. Guo, A. Baker, J. Guo, C. A. Randall, *J. Am. Ceram. Soc.* **2016**, *99*, 3489; b) J. Guo, H. Guo, D. S. B. Heidary, S. Funahashi, C. A. Randall, *J. Eur. Ceram. Soc.* **2017**, *37*, 1529.
- [18] J.-H. Seo, Z. Fan, H. Nakaya, R. Rajagopalan, E. D. Gomez, M. Iwasaki, C. A. Randall, *Jpn. J. Appl. Phys.* **2021**, *60*, 037001.
- [19] S. Bang, A. Ndayishimiye, C. Randall, *Acta Materialia* **2019**, 3428070.
- [20] Y. Liu, J. Liu, Q. Sun, D. Wang, K. R. Adair, J. Liang, C. Zhang, L. Zhang, S. Lu, H. Huang, X. Song, X. Sun, *ACS Appl. Mater. Interfaces* **2019**, *11*, 27890.
- [21] J.-H. Seo, H. Nakaya, Y. Takeuchi, Z. Fan, H. Hikosaka, R. Rajagopalan, E. D. Gomez, M. Iwasaki, C. A. Randall, *J. Eur. Ceram. Soc.* **2020**, *40*, 6241.
- [22] B. He, S. Kang, X. Zhao, J. Zhang, X. Wang, Y. Yang, L. Yang, R. Liao, *Molecules* DOI: 10.3390/molecules27196756.
- [23] a) H. Liu, X.-B. Cheng, J.-Q. Huang, H. Yuan, Y. Lu, C. Yan, G.-L. Zhu, R. Xu, C.-Z. Zhao, L.-P. Hou, C. He, S. Kaskel, Q. Zhang, *ACS Energy Lett.* **2020**, *5*, 833; b) J. Liu, H. Yuan, H. Liu, C.-Z. Zhao, Y. Lu, X.-B. Cheng, J.-Q. Huang, Q. Zhang, *Adv. Energy Mater.* **2022**, *12*, 2100748.

- [24] Y.-C. Lan, M. Ghasemi, S. L. Hall, R. A. Fair, C. Maranas, R. Shi, E. D. Gomez, *ChemSusChem* **2024**, *17*, e202301920.
- [25] Y.-C. Lan, P.-H. Lai, B. D. Vogt, E. D. Gomez, *ACS Energy Lett.* **2024**, *9*, 3324.
- [26] T. Famprikis, P. Canepa, J. A. Dawson, M. S. Islam, C. Masquelier, *Nat. Mater.* **2019**, *18*, 1278.
- [27] a) A. R. Symington, M. Molinari, J. A. Dawson, J. M. Statham, J. Purton, P. Canepa, S. C. Parker, *J. Mater. Chem. A* **2021**, *9*, 6487; b) S. Peng, Y. Chen, X. Zhou, M. Tang, J. Wang, H. Wang, L. Guo, L. Huang, W. Yang, X. Gao, *J. Materomics* **2024**, *10*, 1214.
- [28] K. Takashima, Y. Iwazaki, C. A. Randall, *Jpn. J. Appl. Phys.* **2021**, *60*, 126505.
- [29] J. Guo, S. S. Berbano, H. Guo, A. L. Baker, M. T. Lanagan, C. A. Randall, *Adv. Funct. Mater.* **2016**, *26*, 7115.
- [30] H. Yan, W. R. Cannon, D. J. Shanefield, *Ceram. Int.* **1998**, *24*, 433.
- [31] W. J. Kwon, H. Kim, K.-N. Jung, W. Cho, S. H. Kim, J.-W. Lee, M.-S. Park, *J. Mater. Chem. A* **2017**, *5*, 6257.
- [32] Y. Inaguma, C. Liquan, M. Itoh, T. Nakamura, T. Uchida, H. Ikuta, M. Wakihara, *Solid State Commun.* **1993**, *86*, 689.
- [33] a) S. Sasano, R. Ishikawa, K. Kawahara, T. Kimura, Y. H. Ikuhara, N. Shibata, Y. Ikuhara, *Appl. Phys. Lett.* **2020**, *116*, 043901; b) H. Leng, J. Huang, J. Nie, J. Luo, *J. Power Sources* **2018**, *391*, 170.
- [34] W. Zhao, J. Yi, P. He, H. Zhou, *Electrochem. Energy Rev.* **2019**, *2*, 574.
- [35] S. Wenzel, T. Leichtweiss, D. Krüger, J. Sann, J. Janek, *Solid State Ion.* **2015**, *278*, 98.
- [36] a) S. Wenzel, S. J. Sedlmaier, C. Dietrich, W. G. Zeier, J. Janek, *Solid State Ion.* **2018**, *318*, 102; b) S. Wenzel, D. A. Weber, T. Leichtweiss, M. R. Busche, J. Sann, J. Janek, *Solid State Ion.* **2016**, *286*, 24.
- [37] Z. Jiang, S. Wang, X. Chen, W. Yang, X. Yao, X. Hu, Q. Han, H. Wang, *Adv. Mater.* **2020**, *32*, 1906221.
- [38] M. Du, Y. Sun, B. Liu, B. Chen, K. Liao, R. Ran, R. Cai, W. Zhou, Z. Shao, *Adv. Funct. Mater.* **2021**, *31*, 2101556.
- [39] X.-B. Cheng, R. Zhang, C.-Z. Zhao, F. Wei, J.-G. Zhang, Q. Zhang, *Adv. Sci. (Weinh)* **2016**, *3*, 1500213.
- [40] J. T. S. Irvine, D. C. Sinclair, A. R. West, *Adv. Mater.* **1990**, *2*, 132.
- [41] W. D. Callister, D. G. Rethwisch, *Materials Science and Engineering : An Introduction*, Wiley, Hoboken, NJ **2018**.
- [42] P. Vadhva, J. Hu, M. J. Johnson, R. Stocker, M. Braglia, D. J. L. Brett, A. J. E. Rettie, *ChemElectroChem* **2021**, *8*, 1930.

Manuscript received: September 25, 2024

Revised manuscript received: November 25, 2024

Accepted manuscript online: December 3, 2024

Version of record online: December 10, 2024